International Journal of Multiphase Flow 154 (2022) 104153

Contents lists available at ScienceDirect

International Journal of Multiphase Flow

journal homepage: www.elsevier.com/locate/ijmulflow

Force on inertial particles crossing a two layer stratified turbulent/non-turbulent interface

Marco Boetti *, Lilly Verso

Turbulence Structure Laboratory, School of Mechanical Engineering, Tel Aviv University, Tel Aviv 69978, Israel

ARTICLE INFO

Keywords:
Turbulent/non-turbulent density interfaces
Particles motion
Stratification force

ABSTRACT

We study the peculiar motion of inertial solid particles across stratified turbulent/non-turbulent interfaces (STNTI). Previous studies in quiescent stratified layers demonstrated that inertial particles slow down substantially due to an additional force term related to the stratification. Here we report for the first time a similar effect on inertial particles moving across a two-layer STNTI of finite thickness. This problem is addressed both experimentally and numerically: we utilize the three-dimensional particle tracking velocimetry (3D-PTV) in a index-matched STNTI experiment under an oscillating grid, and two direct numerical simulation (DNS) cases of STNTI. The DNSs test the effects of different turbulent forcings on inertial spheres in the turbulent layer and across STNTI and extends the parameter ranges of Reynolds and Froude numbers unfeasible in the experiments. Turbulence is produced in the DNSs using a convective forcing (heat source at the domain boundary) in one case, and a forcing that mimics a vertically oscillating grid in the other. The numerical spheres are tracked, through one-way coupling approach, using a modified Basset–Boussinesq–Oseen equation which includes a stratification-induced term. The stratification force is modelled as an additional buoyancy of a caudal wake with varying density. This algorithm creates Lagrangian trajectories that resemble the motion of inertial particles across stratified interfaces in quiescent and turbulent experiments. Furthermore, numerical results for the STNTI cases help to distinguish the essential features observed in the experiments that are caused by stratification from those that relate to turbulence–particle interactions.

1. Introduction

Settling of solid spheres through density interfaces is a fundamental process in problems of dispersion, mixing and clustering in stratified environments (Woods, 1995; Camassa et al., 2019; Ardekani et al., 2017). The correct estimate of particles settling velocity in stratified environments is necessary to predict and quantify dispersion of pollutants in the atmosphere (Turco et al., 1983), aggregation of plankton (Turco et al., 1983; MacIntyre et al., 1995), transport of impurities in the ocean's thermocline (Camilli et al., 2010; Camassa et al., 2013).

It is well documented that particles moving across gradients of fluid density have smaller settling velocity v^* than in an equivalent homogeneous density fluid (Yick et al., 2009; Candelier et al., 2014; Mandel et al., 2020; Verso et al., 2019). In particular, when particles cross an interfacial layer of finite thickness between two stratified quiescent regions (the so-called "sharp" stratification case), they assume a distinct behaviour, as observed in experimental (Srdić-Mitrović et al., 1999; Mandel et al., 2020; Verso et al., 2019) and numerical studies (Bayareh et al., 2013; Deepwell et al., 2021). After entering into the stratified layer the particles slow down until they reach a minimum velocity $v_{\min}$, and in some specific conditions they may also be subject to levitation effects (Abaid et al., 2004). The location of $v_{\min}$ was experimentally observed to be close to the outer edge of the interfacial layer (Srdić-Mitrović et al., 1999; Mandel et al., 2020; Verso et al., 2019). After the point of minimal velocity, particles accelerate converging to the terminal velocity of the second fluid layer. This peculiar motion was observed in the range of $1 < Re_{in} < 60$ and $2 < Fr_{in} < 26$ (Abaid et al., 2004; Srdić-Mitrović et al., 1999; Pierson and Magnaudet, 2018; Verso et al., 2019). $Re_{in} = v^*_{in} a/\nu$ and $Fr_{in} = v^*_{in}/(Na)$ are the particle Reynolds and Froude numbers respectively. The subscript "in" refers to the initial fluid layer in which the particle is released, a is the particle diameter, ν the kinematic viscosity and $N = \left(2g|\rho_{in} - \rho_{fin}|/(\rho_{in} + \rho_{fin})h\right)^{1/2}$ the Brunt–Väisälä frequency, determined using density of the two layers and the thickness of the interface h.

This particular behaviour is commonly attributed to an additional force, that has no relevant effect in homogeneous density layers. Hereinafter we refer to it as the stratification force F_S, which is a supplemental term of the Basset–Boussinesq–Oseen equation whose main

* Corresponding author.
E-mail address: marcoboetti@mail.tau.ac.il (M. Boetti).

https://doi.org/10.1016/j.ijmultiphaseflow.2022.104153
Received 13 January 2022; Received in revised form 26 April 2022; Accepted 1 June 2022
Available online 9 June 2022
0301-9322/

components are the drag, buoyancy, added mass, history forces (Geller et al., 1986; Eames and Hunt, 1997; Srdić-Mitrović et al., 1999; Magnaudet and Mercier, 2020; Verso et al., 2019). The nature of F_S has been investigated using both linear stratification and sharp interfacial layers. Experimental studies and subsequent numerical models, have found that in linearly stratified fluids F_S is well reproduced as a drag term (Yick et al., 2009; Candelier et al., 2014; Doostmohammadi et al., 2014; Zvirin and Chadwick, 1975). However, when applied to the sharp interfacial stratification, the additional drag models do not recreate the slow-down effect correctly (Verso et al., 2019). Originating from this discrepancy, an alternative description of F_S is developed: it is modelled as a buoyancy-induced term whose physical interpretation rely on the interaction between the particle and the fluid that tends to stick to it forming a wake (Verso et al., 2019).

There are several examples, such as the oceans and the atmosphere (Riley and Lelong, 2000), in which stratified fluids can interact with turbulence in the form of stratified turbulent/non-turbulent interface (STNTI) flows. Inertial particles then, may be affected by the fluid motion while crossing the stratification. They indeed present, when moving through a turbulent region, different dynamics depending on how strong their inertia is in relation to the fluid agitation. Three distinct regimes can be identified using the parameter $\sigma = U_s/v^*$, that expresses how vigorous the flow is in respect to the particle inertia (Stout et al., 1995), and it can be linked to the Rouse number (Michallet and Mory, 2004; Dejoan and Monchaux, 2013) as $Rou = 1/\sigma$. Being U_s a velocity scale of the fluid. When $\sigma \ll 1$, the particles tend to the "eddy crossing" regime, corresponding to heavy particles falling in a weak turbulent motion: they pass through it with little to no perturbation. The intermediate regime, $\sigma \approx 1$, is called "preferential sweeping". These are particles with moderate inertia that tend to be repulsed away from the turbulent eddies. This behaviour is often referred to as "preferential concentration" to indicate that particles accumulate into specific fluid regions, namely the low vorticity areas (Squires and Eaton, 1991). When $\sigma \gg 1$, the spheres have little inertia, are largely carried by turbulent eddies and they tend toward the "suspension" in the turbulent flow.

The addition of non-trivial flow, and in particular turbulence, complicates the problem not only from a theoretical point of view (at the TNTI, for instance, takes place the turbulent entrainment mechanism) but also from the technical one. Due to the high complexity of the system (i.e. coupling the Lagrangian particles and the Eulerian flow field), experiments usually focus on particles settling in quiescent flows only.

The aim of this study is to investigate the interaction of inertial particles with stratification and turbulence in STNTI flows, with particular attention whether their distinctive dynamics in sharp stratified layers undergoes through changes caused by the fluid agitation.

We then develop a two-layer stably stratified experimental system with turbulence generated by an oscillating grid and enforced mass conservation using multiple pumps (Verso et al., 2017). With this setup we could obtain an index-matched, steady-state, long time stable STNTI across which a sufficient amount of Lagrangian trajectories were retrieved using the three-dimensional particle tracking velocimetry (3D-PTV) (Verso, 2020; Shnapp et al., 2019). Unfortunately, the parameter range of the experiments is limited, and we could not retrieve the flow properties simultaneously with the Lagrangian particles acquisition with the 3D-PTV. Therefore, not all contributions of each force component on the particle could be extracted directly (Traugott et al., 2011; Meller and Liberzon, 2016).

To obtain information about the flow and to extend the parameters range, both in terms of particles and accessible flow cases, we relied on a numerical approach. Two direct numerical simulations (DNS) of a STNTI flow are implemented: in the first one turbulence is generated by a convective forcing through a boundary buoyancy flux, while in the second one using a mechanical forcing (Boetti et al., 2021), analogous to a vertically oscillating grid (Verso et al., 2017, 2019). To model the Lagrangian particles with a one-way coupling approach (Elghobashi, 1991), we utilize a ordinary differential equation (ODE) system based on state-of-the-art numerical Lagrangian tracker (Lange and van Sebille, 2017) with a modified equation of motion. We introduce a new phenomenological formulation for the F_S term, that is validated with experimental results in quiescent stratified flow (Srdić-Mitrović et al., 1999; Verso et al., 2019), resolving the limitations of the previous parametric model (Verso et al., 2019). Even though a direct comparison with the STNTI experiments is not feasible because of the structural differences between the DNS and the experimental flow setup, numerical inertial particles present common features with the results from the experiments, strengthening the model reliability and providing insights on the behaviour of particles settling through STNTIs.

2. Methods and materials

2.1. Experiments

The experimental setup and the measurements have been discussed in details in Verso et al. (2017, 2019), Verso (2020), and are presented here briefly for the sake of clarity.

We measured Lagrangian trajectories of settling and rising particles traversing a STNTI of thickness $h \approx 7.5$ mm ($h/a \sim 10$) using a refractive index matched water–salt–ethanol solution. The experiments were carried out in a glass tank with a 200×200 mm^2 cross-section and a depth of 300 mm (Verso et al., 2017), shown schematically in Fig. 1a. The aqueous mixture of ethanol of density $\rho_1 = 995$ kg m^{-3} is on top of the denser saline solution of Epsom salts and water of density $\rho_2 = 1020$ kg m^{-3}, creating a stable stratification with discontinuity at depth of $z_1 \approx 138$ mm below the free surface. The fluid is agitated mechanically by a vertically oscillating grid with a fixed frequency $f = 4$ Hz and a stroke length $s = 20$ mm. The oscillating grid of size 190 mm^2, with square bars of 5 mm, mesh size $M = 25$ mm and solidity of 38%, is located at a position $z_{g_0} = 65$ mm from the free surface level. Two additional pumps supply volumetric flow rates of 40 ml/min to the bottom and top layers to preserve constant depth and density.

Prior to the Lagrangian experiments with the particles, we measured the turbulent flow field under the oscillating grid using the particle image velocimetry (PIV). A snapshot of the average vertical flow field is presented in Fig. 1b providing a qualitative overview of the motion generated in the tank. Due to the impossibility to overlap the two optical techniques, 3D-PTV and PIV, the Eulerian velocity field measurements were not collected simultaneously with the Lagrangian tracking of particles, preventing a direct analysis of the particle–fluid interaction. Nevertheless, PIV measurements provide general knowledge of the background turbulent flow characteristics. The Taylor Reynolds number in the turbulent region is estimated using the model of Long for oscillating grids (Long, 1978; Verso et al., 2017) $Re_\lambda = \sqrt{2k/3}\lambda/\nu \approx \sqrt{15K_g/\nu} = 58$, being $k = 1/2(u'^2 + v'^2 + w'^2)$ the turbulent kinetic energy, λ the Taylor lengthscale and $K_g = u'_{RMS}|z - z_{g_0}|$ the grid-action parameter that depends on the distance from the grid $|z - z_{g_0}|$ and the root mean square (RMS) of the horizontal velocity fluctuations u'_{RMS}. The Schmidt number of the two fluid regions is $Sc_1 = \nu_1/D_1 \approx 880$ for the top turbulent layer and $Sc_2 = \nu_2/D_2 \approx 1660$ for the bottom layer, being ν and D the kinematic viscosity and mass diffusivity of each region. The bulk Richardson number is estimated as $Ri = (\Delta b L)/{u'_{RMS}}^2 = 100$, being Δb the buoyancy difference between the two layers.

Four different types of inertial solid particles, named $P_1 - P_4$ are used in the experiments. They are manufactured in polystyrene (P_1, P_2 and P_3) and soda-lime glass (P_4), with a spanning range of both diameter and density, the exact specifics are reported in Verso et al. (2019). In addition to these, the data from Srdić-Mitrović et al. (1999) used in the present work is marked with P_F. The particles, whose main physical characteristics are reported in Table 2, were released in the centre of the tank in the area marked with PTV in Fig. 1b. For the

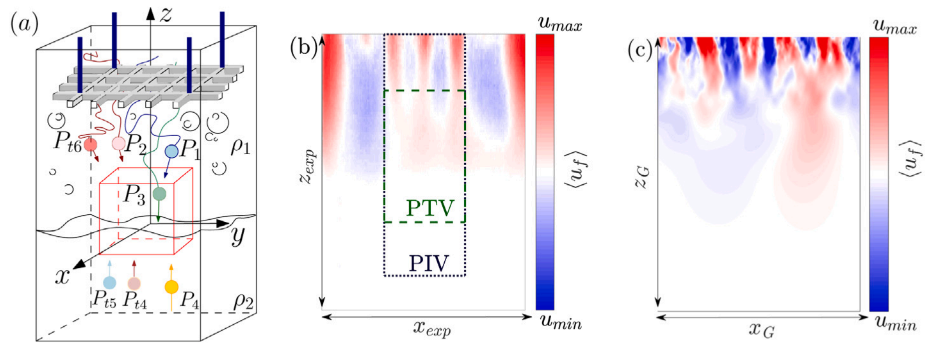

Fig. 1. (a) Sketch of the oscillating grid experimental system of Verso et al. (2017) with marked 3D-PTV measurement region (red area). (b) Measured mean velocity field of the oscillating grid experiment (with PIV and PTV measurement areas marked) and (c) mean vertical velocity field of the DNS of the grid flow. Note that: $x_{exp} \approx 4/3 x_G$, $z_{exp} \approx z_G$. (For interpretation of the references to colour in this figure legend, the reader is referred to the web version of this article.)

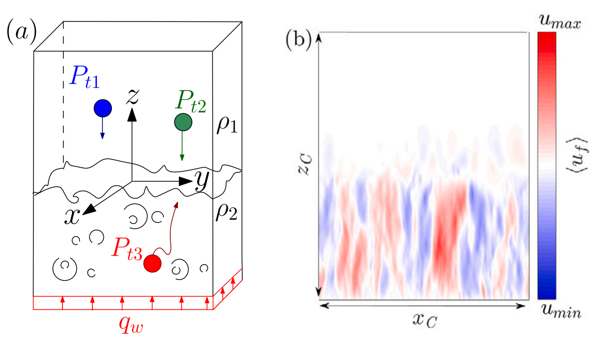

Fig. 2. (a) Sketch of the convective turbulence setup studied in Boetti et al. (2021). (b) Mean vertical velocity field of the DNS of the convective turbulence. Note that: $x_C = 4x_G \approx 3x_{exp}$, $z_C = 2z_G \approx 2z_{exp}$.

Lagrangian measurements, we use the 3D-PTV with the OpenPTV open source software to obtain the particle Lagrangian trajectories (Shnapp et al., 2019; OpenPTV consortium, 2014) and the observation control volume measures $20 \times 20 \times 50$ mm^3, Fig. 1a–b.

2.2. Direct Numerical Simulations (DNS)

The DNSs are performed using SPARKLE code (van Reeuwijk et al., 2008a,b), which integrates the incompressible Navier–Stokes equations with the Boussinesq approximation. The system of equations, comprising of linear momentum, mass conservation, and buoyancy diffusion with the condition of incompressible flow, are reported as follows:

$$\frac{\partial u_i}{\partial t} + u_j \frac{\partial u_i}{\partial x_j} = -\frac{1}{\rho_0}\frac{\partial p}{\partial x_i} + \nu \frac{\partial^2 u_i}{\partial x_j^2} + b\delta_{i3} \tag{1}$$

$$\frac{\partial b}{\partial t} + u_j \frac{\partial b}{\partial x_j} = \kappa \frac{\partial^2 b}{\partial x_j^2} \tag{2}$$

$$\frac{\partial u_i}{\partial x_i} = 0 \tag{3}$$

where u_i (with $i, j = 1, 2, 3$ representing respectively the horizontal directions x, y and the vertical direction z) is the velocity vector, $b = g(\rho_0 - \rho)/\rho_0$ is the buoyancy, ν is the kinematic viscosity and κ the thermal diffusivity (the Prandtl number is set to $Pr = \nu/\kappa = 1.25$ throughout the domain), g is the gravitational acceleration and ρ_0 is a reference density.

The code is fully parallelized, making use of the domain decomposition in two directions. The spatial differential operators are discretized using second-order symmetry preserving central difference (Verstappen and Veldman, 2003) and time integration is carried out with an adaptive second-order Adams–Bashforth method (van Reeuwijk et al., 2008a). Periodic boundary conditions are applied to the lateral walls and free-slip conditions to the upper and bottom boundaries of the domain. At the initial instant $t = 0$, the fluid is quiescent, thus the setup is a two-layer stratification with its interface at the domain middle position $z = L/2$. We set ρ_0 as the density of the bottom layer, which implies that $b = 0$ in the bottom half and $b > 0$ in the upper half.

Two different DNS flows (Boetti et al., 2021) are used to track numerical particles whose parameters are set to develop a well-mixed turbulent layer up to the initial buoyancy discontinuity.

The first one is a grid-generated turbulent flow (case **G**) in a cuboidal domain of size $L_x \times L_y \times L_z = L/2 \times L/2 \times L$, with a $360 \times 360 \times 720$ mesh. The oscillating grid is implemented using a standard immersed boundary method, with the grid position of the form:

$$z_g(t) = z_{g0} + \frac{s}{2}\sin(2\pi f t) \tag{4}$$

$z_{g0} = 2/3L$ from the bottom of the domain and its velocity $\mathbf{u}_{grid} = (0, 0, dz_g/dt)$ is imposed to the domain in the region occupied by the grid. The incompressibility of the fluid is preserved by calling the Poisson solver for pressure right after the computation of $z_g(t)$ and $\mathbf{u}_{grid}$. Other key parameters of the oscillating grid are the stroke length $s/L = 0.07$, and the dimensionless oscillation frequency $ft_* = 42$, being $t_* = l/u'_{RMS}$ the turnover time, u'_{RMS} the RMS of horizontal velocity fluctuations, and l the integral lengthscale. The square grid bars have thickness and mesh size of $0.016L$ and $0.06L$ respectively. Since the fluid velocity in the region above $z > z_{g0} - s/2$ ($\approx 1.5h + z_I$) is directly affected by the oscillating grid motion, the corresponding volume is excluded from the analysis in the following sections. The resulting flow is shown in Fig. 1c with a snapshot of the vertical velocity field.

The second DNS, whose sketch is reported in Fig. 2a, is a convective flow (case **C**) simulated with a constant vertical heat flux $q_w = -\kappa\partial\theta/\partial z$ applied at the bottom boundary, being β the thermal expansion coefficient and θ the temperature. The three-dimensional volume has $L_x \times L_y \times L_z = 2L \times 2L \times L$ size, with a computational resolution of $N_x \times N_y \times N_z = 720 \times 720 \times 360$ nodes. Similarly to **G**, this case also develops a fully mixed region between the turbulence source at the boundary and the initial density jump at $L_z = L/2$ as evident in the vertical velocity snapshot reported in Fig. 2b.

Despite the similarities, the two DNSs present an important difference in their turbulent forcing mechanisms: case **C** produces turbulence via the buoyancy flux over the entire mixed layer (ML), while for the grid case **G**, the turbulence is generated at the grid location and then transported through the ML (Boetti et al., 2021). The consequence of this difference is that the turbulence intensity of the ML in **C** is roughly constant throughout the whole layer, while case **G** presents a rapid decay of turbulence intensity right below the region of the direct agitation by the oscillating grid.

All the metric of the DNSs (as well as the Lagrangian tracking results in Section 4) are computed after the ML is fully developed and the system has reached a quasistationary condition. Details of **G** and **C** are

Table 1
The DNS cases main features and metrics.

	$N_x\ N_y\ N_z$	$L_x\ L_y\ L_z/L^3$	Pr	Re_λ	Ri	Ra	Δ_L/η
C	$720^2\times 360$	$2^2\times 1$	1.25	44	240	$1.3\ 10^8$	0.91
G	$360^2\times 720$	$0.5^2\times 1$	1.25	35	30	$1.8\ 10^8$	2.2

Table 2
Properties of particles. P_1, P_2, P_3, P_4 and P_F: quiescent and TNT experimental fluid flow. Numerical particles released in stratified TNT flows: P_{1t}, P_{2t}, P_{3t} (case **C**); P_{4t}, P_{5t}, P_{6t} (case **G**). For experimental particles density, Froude and Reynolds numbers correspond to $\rho\equiv\rho_2$, $Re\equiv Re_2$, $Fr\equiv Fr_2$ the bottom layer values in the quiescent flow. Simulations: $\rho\equiv\rho^*$, $Re\equiv Re^*$, $Fr\equiv Fr^*$ are the values in the quiescent layer for the TNTI flows. $\langle\sigma\rangle$ reports the mean value in the turbulent layer.

	P_1	P_2	P_3	P_4	P_F	P_{1t}	P_{2t}	P_{3t}	P_{4t}	P_{5t}	P_{6t}
$\langle h\rangle/a$	14.5	28.7	16.4	16.9	15.9	20.4	27.8	15.6	27.0	10.1	10.1
ρ_p/ρ	1.03	1.19	2.42	0.93	1.01	1.15	3.04	0.76	0.71	0.38	1.43
Re	6.5	6.0	84.2	9.6	1.3	13.8	81.6	19.2	21.6	212	168
Fr	1.3	4.8	22.3	2.8	0.5	3.8	22.2	4.5	5.2	8.1	6.3
$\langle\sigma\rangle$	0.32	0.36	0.042	1.16	–	1.8	0.17	0.58	1.4	0.35	0.44

summarized in Table 1: $N_{i=x,y,z}$ and $L_{i=x,y,z}$ represent the computational and physical domain sizes respectively. The Taylor microscale Reynolds number, $Re_\lambda = \sqrt{2k/3}\lambda/\nu$, is computed into the mixed layer at $(z-z_I)/h \approx 1.5$. We report the bulk Richardson and Rayleigh numbers as $Ri = \Delta bL/2k$ and $Ra = \Delta bL^3/8\nu\kappa$ to estimate of the strength of the stratification and convection in the DNSs. In addition to these measures, the Nusselt number for case **C** is assessed as $Nu = 2q_w/\Delta\theta\kappa L = 9.5\ 10^2$. Table 1 reports also the maximum ratio between computational domain mesh size Δ_L and the Kolmogorov lengthscale η at $(z-z_I)/h \approx 1.5$, indicating that the grid resolution is small enough to capture small scales in both cases **C** and **G**.

We track Lagrangian particles with a one-way coupling approach (Elghobashi, 1991), using the 3D snapshots retrieved from the turbulent flows simulated with SPARKLE, integrating the equation of motion described in Section 3, using a customized code based on the open source Lagrangian simulator PARCELS (GitHub repository, web-site page) (Lange and van Sebille, 2017; McAdam and van Sebille, 2018).

3. The model

The motion of spherical particles in the homogeneous density layer is well described by Maxey and Riley (1983). In the parameters space of Verso et al. (2019), both the added mass and history forces are negligible, then the equation of motion is simplified as:

$$m_p\frac{d\mathbf{v}}{dt} = \mathbf{F}_B + \mathbf{F}_D + \mathbf{F}_S \tag{5}$$

The buoyancy force is defined as $\mathbf{F}_B = (\rho_p-\rho_f)V_p\mathbf{g}$, where ρ_p, ρ_f and V_p are respectively the particle density, the fluid density (sampled at the particle position), and the particle volume expressed as $V_p = \pi a^3/6$. The viscous drag force is defined as $\mathbf{F}_D = \frac{1}{2}C_D\rho_f A_p|\mathbf{v}_{rel}|\mathbf{v}_{rel}$, where $\mathbf{v}_{rel} = \mathbf{v}-\mathbf{u}_f$ is the relative velocity between the particle and the fluid, $A_p = \pi a^2/4$ is the particle projected area. The drag coefficient included in $\mathbf{F}_D$ is based on the non-linear model $C_D = 0.4{+}24/Re{+}6/(1{+}Re^{1/2})$ (White, 2006). $\mathbf{F}_S$ is the additional term associated with stratification that is described in Section 3.1. The evolution of the components of Eq. (5) through a stratified quiescent flow for particle type P_1 is reported in Fig. 3a.

3.1. The stratification force

The stratification force model is developed using (Verso et al., 2019) as benchmark: the algorithm is improved making it more flexible, reducing the number of input parameters and the constraining factors that would limit its use in cases different from the ones presented in Verso et al. (2019).

We first reduce the use of general flow parameters substituting them with local ones. Hence the relevance of knowing 'a priori' variables in the second layer while integrating the ODE system greatly diminishes. The expression of F_S is modified too: the dependency on the density interface h (which is needed as input parameter in Verso et al. (2019)) is eliminated. Then F_S behaviour does not rely on conditional statements, as showed in the inset of Fig. 3a. In the current model the stratification force is in fact a continuous function that acts with a more direct effect from the local flow conditions, affecting the particles not only within the large scale discontinuity h but also from local gradients in the density field, such as the plumes and eddies in STNTI flows.

$\mathbf{F}_S$ is then interpreted as an additional buoyancy contribution to the particle equation of motion by a fluid wake of constant volume that remains attached to the particle and continuously exchanges fluid with the surroundings:

$$\mathbf{F}_S = (\rho_{\mathrm{cw}}-\rho_f)V_{\mathrm{cw}}\mathbf{g} \tag{6}$$

where V_{cw}, ρ_{cw} are respectively the caudal wake volume and its density. The caudal volume dragged by the particles was found empirically in Verso et al. (2019) as $V_{\mathrm{cw}} = 0.13V_pFr_{in}^{3/4}$. The density of the wake ρ_{cw}, whose temporal evolution is showed in Fig. 3b, is modelled in differential form as:

$$\frac{d\rho_{\mathrm{cw}}}{dt} = \frac{\rho_f(t-\tau_{\mathrm{cross}})-\rho_{\mathrm{cw}}}{\tau_{\mathrm{rec}}} \tag{7}$$

where τ_{cross} and τ_{rec} are respectively the crossing and the recovery times.

τ_{cross} represents the temporal interval between the entrance into the interfacial layer and the exit from it. The crossing time is strongly correlated to the time τ_{min} when minimal velocity is reached, even though some discrepancies between the two may be present, as discussed in Verso et al. (2019). Then τ_{cross} is computed using Eq. (8) as proposed by Srdić-Mitrović et al. (1999) to define τ_{min}:

$$\tau_{\mathrm{cross}} \approx \tau_{\mathrm{min}} = \beta Re_{in}^m\ a^2/\nu_{in} \tag{8}$$

where $\beta = 140$ and $m = -1.7$ are empirical constants (Srdić-Mitrović et al., 1999).

The recovery time was first formulated empirically by Verso et al. (2019) as the time needed by the particle to recover its terminal velocity in the second layer after it reached the minimal velocity (or equivalently, the time F_S takes to dissipate once the particle has exited the stratified interface). In its original formulation in Verso et al. (2019), τ_{rec} was expressed as function of the second fluid layer properties, as: $\tau_{\mathrm{rec}} \approx 13Re_{fin}^{-1}\ a^2/\nu_{fin}$. In this study τ_{rec} is modified using local variables, as already mentioned, being $Re \equiv Re(v(\mathbf{x}_p(t)), \nu(\mathbf{x}_p(t)))$, $\nu \equiv \nu(\mathbf{x}_p(t))$, with v the vertical component of the particle velocity $\mathbf{v}$ (being $v = \mathbf{v}\cdot\hat{\mathbf{z}}$):

$$\tau_{\mathrm{rec}} = 13Re^{-1}\ a^2/\nu = 13a/v \tag{9}$$

τ_{rec} is then related to the fluid flow rate inside the wake as $V_{cw}/vA_p \sim a/v \propto \tau_{rec}$.

3.2. Particles motion in quiescent stratified fluid

In order to validate the new algorithm, we now present a comparison between experimental and numerical results of particles moving across a two-layer stratified quiescent fluid with an interface thickness $h/a \sim 10$.

Particles of family P_1, P_3, P_4, P_F (Verso et al., 2019), whose properties are reported in Table 2, are used as reference. In Fig. 4 we show the mean vertical velocity of the experiments, the results of the F_S model developed in Verso et al. (2019) (*VVL19* model), and finally the outputs of the current model, discussed in Section 3.1. The velocity profiles are normalized using the terminal velocity of the initial layer in which the spheres are released. Results are shown as function of the vertical coordinate $(z-z_I)/h$, being the interface upper and lower

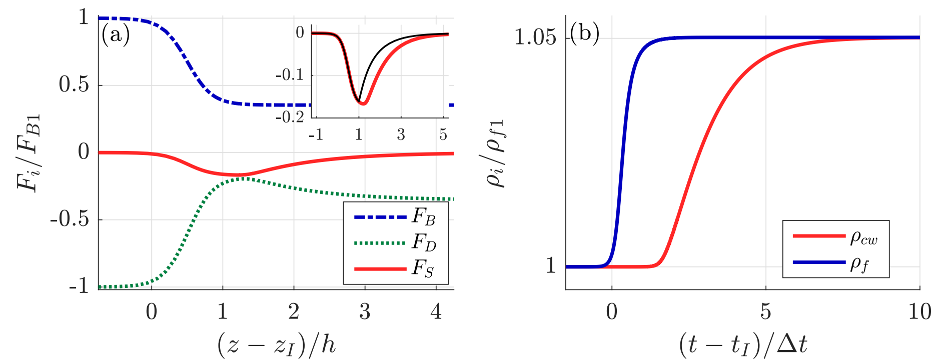

Fig. 3. Force components for the P_1 type: (a) vertical profiles of buoyancy F_B, drag F_D (vertical component), stratification F_S forces. Inset: F_S vertical profile computed with the present study algorithm (red) and Verso et al. (2019) (black) ; (b) temporal evolution of fluid density ρ_f at the particle position and caudal wake density ρ_{cw}. (For interpretation of the references to colour in this figure legend, the reader is referred to the web version of this article.)

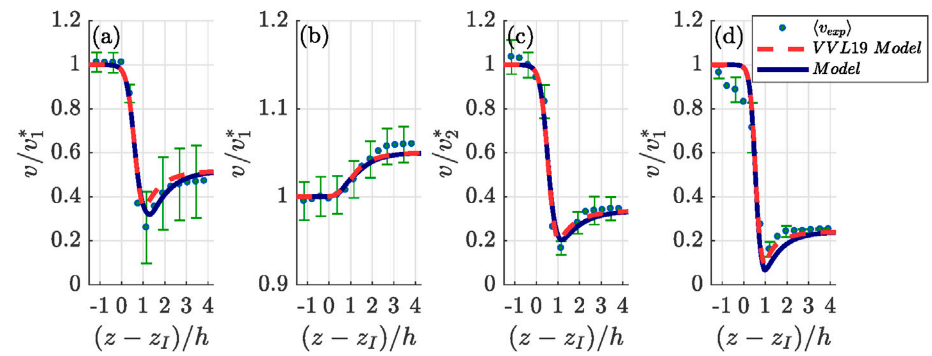

Fig. 4. Vertical velocity profiles of particles (a) P_1, (b) P_3, (c) P_4, (d) P_F. The mean velocity values (green dots) of experiments are compared with two different models: VVL19 (Verso et al., 2019) (red dashed line), current algorithm (blue line). (For interpretation of the references to colour in this figure legend, the reader is referred to the web version of this article.)

boundaries coincident with $z-z_I=0$ and $z-z_I=h$ respectively (Verso et al., 2019). We reconstructed for the two algorithms the density and viscosity vertical profiles of the experiments as hyperbolic tangent functions ($f(z)\propto(1-\tanh z)$), as in Verso et al. (2019).

The new algorithm reproduces the experimental observations with good agreement and reduces the discrepancy between the experiments and the previously modelled results in terms of the minimum velocity magnitude. The location of the minimum velocity $v_{\min}$ predicted by the new algorithm occurs respectively for P_1, P_4, P_F at $(z-z_I)/h=$ [1.28, 1.14, 1.01, i.e. slightly after the exit from the interfacial layer.

Preliminary tests of the new model in linear stratified quiescent flow are also presented in Appendix, along with a qualitative comparison with two drag-based algorithms (Yick et al., 2009; Doostmohammadi et al., 2014). The profiles of F_S and v produced by the three algorithms are actually similar once our model adjusts to the surrounding fluid and forgets the initial conditions.

4. Results

This section reports the results of particles moving across a two-layer stratified TNTI flow. We first show the experimental results and then the outcome of the numerical model in the DNS STNTI flows.

Despite the similarities between the simulations and the experimental flows, a direct comparison is not appropriate because of the intrinsic differences between the two approaches. The main one is that the DNSs have periodic conditions on the lateral boundary while the experimental setup is enclosed by lateral walls. Hence the experimental flow presents a large scale circulation due to these walls. In addition to this, the numerical particles are modelled as spheres while the experimental ones are more variable in shape and size (Verso et al., 2019), making it impossible to create a numerical particle identical to the real one.

4.1. Experimental particles crossing STNTI

The experimental measurements of the Lagrangian particles crossing the STNTI are now presented. The particles, see Table 2, are released at the centre of the tank where the PTV measurement area is set, as mentioned in Section 2.1. They fall (P_1 and P_2) or rise (P_4) through the interface encountering a flow field with the specific pattern produced by the grid and the effect of the tank confinement.

The vertical velocity profiles, normalized by v^* similarly to Section 3.2, are reported in Fig. 5. Note that hereinafter the vertical axis $(z-z_I)/h$ is set such that the quiescent layer corresponds to negative values and the turbulent one to $(z-z_I)/h>1$ respectively. The results clearly indicate that, in the parameters (Re, Fr, h/a) range investigated in the current work, the stratification force occurs and impacts significantly the dynamics of the particle motion in TNTI flow. All the particle types, when entering into the interface layer decelerate considerably till a minimum vertical velocity v_{min}, and after the slow down, the particles accelerate in the second layer.

In Fig. 5a–b are presented the velocity profiles of P_1 and P_2 types respectively. These particles are released in the turbulent upper layer, then they cross the TNTI and settle into the quiescent layer. The analysis of the vertical velocity of particles in Fig. 5a reveals that P_1 have altered mean settling velocity in the turbulent layer. In fact, these particles present a reduced value of the terminal velocity in respect to their steady state mean velocity in the still fluid (with similar fluid density). It can be seen in Fig. 5b that due to their size and density, the spheres of type P_2 have comparable values of the settling velocity in both layers, in agreement with the results of Verso et al. (2019) in quiescent flow. Their slow down is relatively small if compared to the other particle types, being $v_{min}/v^*\sim 0.9$. Eventually, the oscillations in the mean velocity profile and the appearance of local minima inside

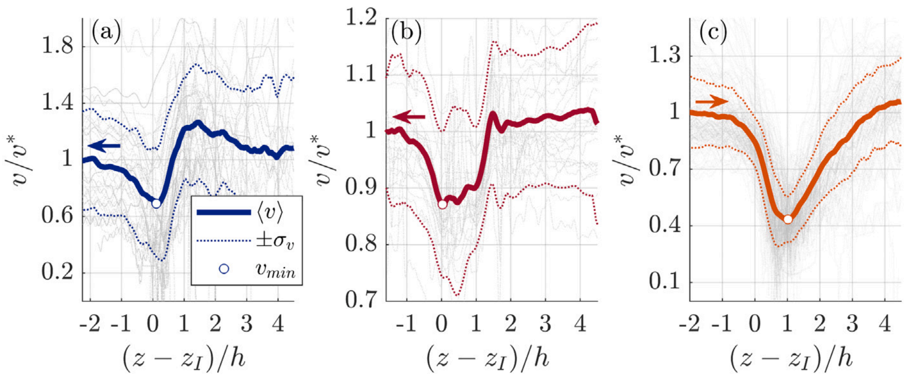

Fig. 5. Experimental vertical velocity profile for particles P_1 (a), P_2 (b), and P_4 (c) types as function of the distance from the interface. The profiles are normalized by the settling velocity of the quiescent region v^*. Particles velocities are reported as light grey, the mean velocity and standard deviation are marked respectively as bold and dashed lines. Dots mark the minimum velocity. Arrows indicate the direction of the motion.

the interface, are likely caused by the lower signal-to-noise ratio in the experimental data.

Fig. 5c reports the vertical velocity of type P_4, they are initially released into the quiescent bottom layer and move upward toward the turbulent one. These particles as well present the slow down due to the stratification and the minimal velocity near the exit of the interfacial region. Then P_4 accelerate into the turbulent layer and their mean vertical velocity increases significantly. This effect is due not only to buoyancy, but also to the fluid motion, being $v(z - z_I \approx 4h) > v^*$. While in the quiescent flow case the spheres of type P_4 reach constant terminal velocity in the upper layer at $z - z_i \approx 2h$, as showed in Fig. 4, in the turbulent flow that the same type of particles continues to accelerate toward the oscillating grid. An additional difference between the settling of P_4 in the quiescent flow and in the turbulent one consists in the magnitude of the minimal velocity. In the latter case $v_{min} \approx 0.4v^*$, that is twice larger than in the experiment without turbulence.

The discrepancies in terminal velocities between the current oscillating grid experiment and the still case presented in Verso et al. (2019), for both P_1 and P_4, strongly suggest that turbulence might affect the dynamics of the particle moving through stratified TNTIs.

4.2. Numerical particles crossing DNS STNTI

In this section is reported the motion of the numerical Lagrangian particles across DNS STNTI flows using the new stratification F_S model.

Every run included 400 spherical particles, see Table 2, randomly generated on a horizontal surface $x - y$, at a fixed height. Three runs, P_{1t}, P_{2t}, P_{3t}, were performed for the DNS case **C**. Particles of type P_{1t} and P_{2t} were released into the quiescent region and settle into the turbulent layer, while P_{3t} type was released in the turbulent layer and rose toward the quiescent zone. Other three runs were performed for DNS case **G**: P_{4t}, P_{5t}, P_{6t}. Particles of type P_{4t} and P_{5t} were released into the quiescent region while P_{6t} moved from the turbulent to the quiescent one.

The vertical velocity profiles for each sphere type are shown in Fig. 6.

The influence of the flow on the particle is measured using the parameter $\sigma = U_s/v^*$, reported in Table 2, with $U_s \equiv \sqrt{k}$. Because some of the particles species lack of a terminal velocity into the turbulent layer, σ is computed using the settling velocity v^* that may result in a underestimation of the σ value for P_{1t}, P_{2t}, P_{4t}, P_{5t}.

For both spheres P_{1t} and P_{4t}, $\langle\sigma\rangle \geq 1$ indicates that the motion is significantly influenced by the turbulent flow. On the other hand, $\langle\sigma\rangle <$ 1 for P_{2t} and P_{5t}, therefore these particle types are less sensitive to the surrounding turbulent flow. Further information can be obtained from the Stokes number $St = t_p/t_f$, being $t_p = |\rho_p - \rho_f|(a/2)^2/18\mu$ and t_f the particle relaxation time and the flow characteristic time respectively. A qualitative comparison between the Stokes number of P_{1t} and P_{2t} for DNS case **C**, and P_{4t} and P_{5t} for case **G**, shows the different influence the particles undergo through the flow: $St_{2t}/St_{1t} = 27$, $St_{5t}/St_{4t} = 17$.

We observed that the spheres of type P_{1t} and P_{4t}, Fig. 6a–b respectively, reach the minimal velocity inside the interface, while for P_{2t} and P_{5t} the location of $v_{\min}$, similarly to the quiescent flow case, occurs after the exit of the interface, $z - z_I \approx \langle h\rangle$. The shift of the minimal velocity position for P_{1t} and P_{4t}, might be caused by the action of the fluid motion overcoming the influence of the stratification. To support this hypothesis, we reported in Fig. 6, for each particle type, the vertical velocity v_q in the quiescent stratified fluid but with the same density profile sampled by $\langle v\rangle$. Both types P_{1t} and P_{4t} actually present a discrepancy in the $v_{\min}$ location between the turbulent flow and the quiescent case. On the contrary, P_{2t} and P_{5t} show similar location of minimum velocity in both turbulent and quiescent flow cases.

Fig. 6e–f report the vertical velocity of spheres released into the turbulent region. The initial values of the parameters τ_{cross} and V_{cw} are taken from the particles stationary conditions in a quiescent layer (i.e. $0 = \mathbf{F}_B + \mathbf{F}_D$). Although this introduces uncertainty in the results, after a relatively short initial adjustment (it takes $\Delta z \approx 0.1\langle h\rangle$ to P_{3t} and $\Delta z \approx 0.2\langle h\rangle$ to P_{6t}), P_{3t}, P_{6t} reach a quasi-constant value of vertical velocity. Indeed, the particles show the well-known behaviour, experiencing the slow down in the stratified layer and reporting the minimum velocity in the proximity of the exit from the interface.

The velocity profiles of P_{1t} and P_{4t}, showed in Fig. 6a–b, present in addition to the v_{min} location, another difference between v_q and $\langle v\rangle$: the latter is larger throughout the turbulent region than the velocity retrieved in the quiescent flow, as already mentioned for P_4 in Fig. 5c and observed in Wang and Maxey (1993). It may be related to the onset of preferential sweeping of P_{1t} and P_{4t} when they approach the turbulent layer: these particles would travel within fluid that moves in the same direction of their settling. Therefore, the stratification-related slow down would be mitigated already into the interfacial region, and once the spheres enter the fully turbulent layer, they continue to accelerate with no evidence of reaching their terminal velocity, as clear in Fig. 6b.

To support this reasoning, we present in Fig. 7 the probability density functions (PDF) of the fluid velocity u_f inside the turbulent region: $1.5 < (z - z_I)/\langle h\rangle < 2$ for case **C** and $1.25 < (z - z_I)/\langle h\rangle < 1.5$ for **G**. The distributions are computed using different subsets: the first one reports the values of u_f throughout the whole DNS sub-domain (marked as $u_{f_{tot}}$ in Fig. 7), the second PDF represents the fluid velocity at the particle position ($u_f(\mathbf{x}_p)$) and lastly we show the PDF of fluid velocity sampled by particles moving in their initial settling direction ($u_f(v/v^* > 0)$).

Particles P_{1t} are reported in Fig. 7a: the PDFs show that the flow with opposite direction than the particles, $u_f/v^* < 0$, is proportionally more frequent in the domain ($u_{f_{tot}}$) than being found by P_{1t} ($u_f(x_p)$). Hence P_{1t} encounter more often parcels of fluid with the same velocity

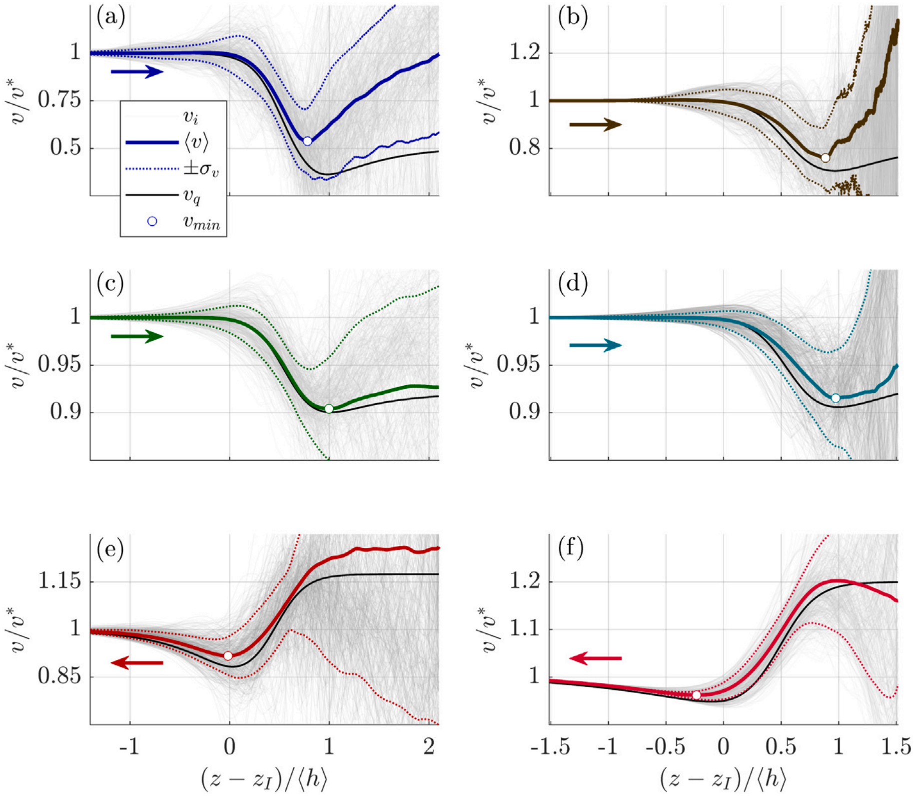

Fig. 6. Normalized vertical velocity as function of the distance from the interface in DNS convective flow **C** (left column) and DNS oscillating grid **G** (right column): (a) P_{t1}, (c) P_{t2}, (e) P_{t3}, (b) P_{t4}, (d) P_{t5}, (f) P_{t6}. Grey lines represent the velocity of each particle, dotted lines represent the standard deviation. White dot marks the minimum velocity. Black curves show the respective quiescent velocity profile. The arrow indicates the direction of the spheres motion.

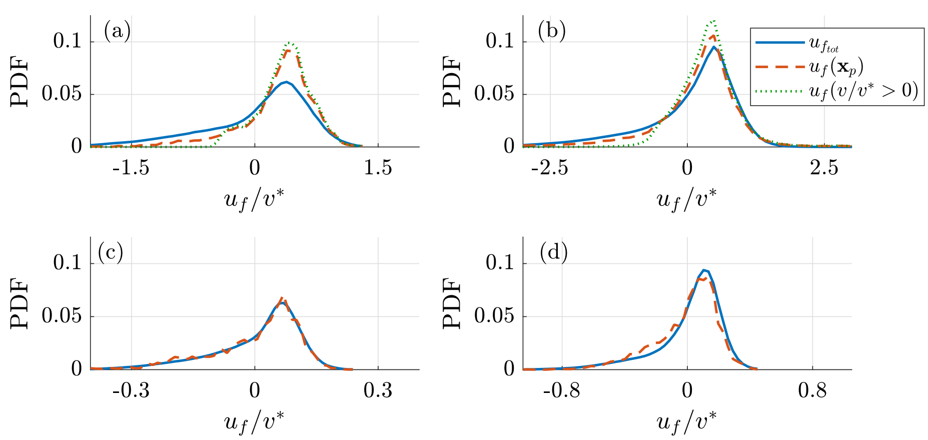

Fig. 7. PDF of flow vertical velocity inside the turbulent layer: (a) P_{1t} in: $z - z_I \in [1.5, 2]\langle h\rangle$; (b) P_{4t} in: $z - z_I \in [1.25, 1.5]\langle h\rangle$; (c) P_{2t} in: $z - z_I \in [1.5, 2]\langle h\rangle$; (d) P_{5t} in: $z - z_I \in [1.25, 1.5]\langle h\rangle$. $u_{f_{tot}}$ (blue) shows the velocity retrieved from the DNS; $u_f(\mathbf{x}_p)$ (red) the fluid velocity sampled by particles and $u_f(v/v^* > 0)$ (green) only for particles moving in the same direction of v^*. (For interpretation of the references to colour in this figure legend, the reader is referred to the web version of this article.)

direction as their initial one, similarly to Wang and Maxey (1993). This characteristic is even more noticeable when looking only at the particles moving toward the turbulent core ($u_f(v/v^* > 0)$) that do not sample any fluid velocity smaller than $-0.5v^*$.

The same behaviour can be seen in Fig. 7b that reports the results for P_{4t}. These particles settle into the turbulent core largely "avoiding" parcels of fluid that move in the opposite direction, being the probability that $u_f(v/v^* > 0)/v^* < -1$ occurs negligible. On the other hand, P_{2t} and P_{5t} present PDFs of $u_f(\mathbf{x}_p)$ more similar to the whole domain distribution, as reported in Fig. 7c–d. It seems that P_{1t}, P_{4t} particles types do not possess enough inertia (as confirmed by their relatively large $\langle\sigma\rangle$) to move through turbulent eddies and cross them undisturbed, just like P_{2t} and P_{5t}, but they follow the flow.

Finally, it can be noticed that the PDFs are not symmetric and the fluid with $u_f/v^* > 0$ is more frequent. This fact depends on the TNTI system construction: the fluid acquires large momentum when near the turbulent forcing that pushes it away (hence $u_f/v^* \ll 0$), and loses gradually momentum by thermal diffusion and kinetic energy dissipation until it is forced again toward the source by the presence of the stratification and other parcels of fluid that come from the turbulent core.

5. Conclusions

Modelling the behaviour of inertial particles as they traverse stably stratified fluids is fundamental in a wide variety of phenomena (Burd

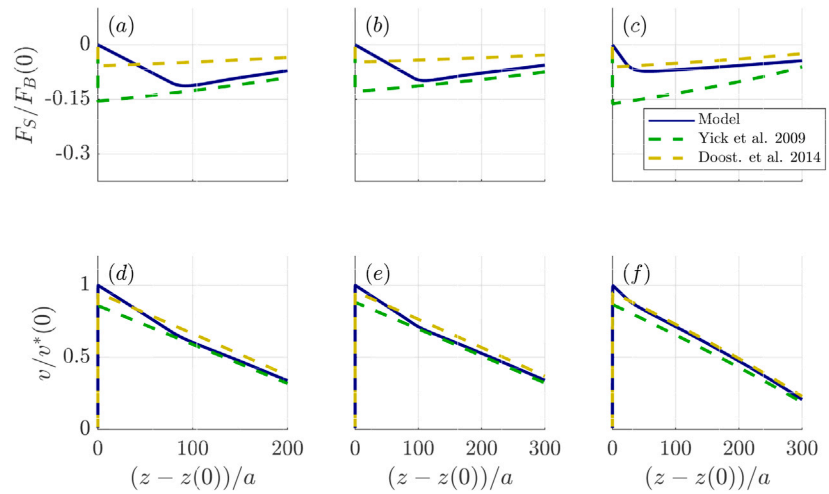

Fig. 8. Comparison of vertical profiles of F_S (a,b,c) and vertical velocity (d,e,f), in linear stratification for different algorithms. Left column: Test A; central column: Test B; right column: Test C, see Table A.3.

and Jackson, 2009; Kok, 2011; MacIntyre et al., 1995; Smith et al., 1992; Turco et al., 1983). However, the motion through a stratified TNTI remained to a large extent unexplored. In this study, we investigated experimentally and numerically the effect of stratification and turbulence on Lagrangian trajectories of inertial particles across a STNTI. The experiments are performed in refractive index match conditions with the interface in a steady-state position. We use Particle Tracking Velocimetry (3D-PTV) measurements, to get the 3D particle time trajectories.

We observed for the first time, that spheres moving in a STNTI flow, experience a stratification-driven force F_S. Analogously to the quiescent stratified layers case, this additional force induces the particles to slow down while crossing the turbulent/non-turbulent interfacial layer.

We propose a new parametric model with the additional force term to the equation of motion based on the stratification effects. The ODE system solves the particle-caudal wake coupling by adding F_S as a buoyancy force for the latter one and it also includes an expression that describes the wake density evolution. Using this approach, we reduce the limitations of previous studies and enable the integration of Lagrangian trajectories in DNSs stratified fluids with non-trivial flows. The new model is validated by comparing it with the experimental data of quiescent stratified flow and a previous parametric model (Verso et al., 2019).

Finally, the model is implemented in two STNTI DNSs: one generated by a convective forcing (with a boundary buoyancy flux), and the other using a mechanical type of forcing (a vertically oscillating grid). Despite the inability to match precisely all experimental flow and particle conditions in the numerical simulations, this is an essential step in our quest to gain deeper insight on the physics of the stratified TNTI flow itself, and on the motion of inertial particles across it. The key result is that the new force model applied to DNS results is able to reproduce, for all sets of parameters, the effects of stratification on particle motion. These effects lead to the minimum of the settling velocity near the edge of the interface.

The model highlights clearly that turbulence affects the motion of the numerical particles by shifting the location of the minimal velocity of low inertia type. Moreover, the same particle species present a growth of their vertical velocity when approaching the turbulent layer. The effect, observed in the experimental data as well, is considered related to the small inertia that causes the channelling into flow areas with the same direction of the particles settling velocity.

The work presented here can serve as a springboard for future studies to provide a more complete picture of the behaviour of particles crossing density interfaces in complex flows. Particular attention should be paid on the origins of the mechanisms presented here and related both to stratification and turbulence. Hopefully more insights on the caudal wake volume "attached" to the particle will be obtained so that further reduction of input parameters may allow to develop a model based only on first-principle theory. New studies should as well focus on detailed inspection of the particle–fluid surroundings to understand the dynamics and evolution of the first one through the interaction with the flow. Finally, more data should be collected on particles settling through different kinds of density interfaces to unify the many distinct models currently available.

CRediT authorship contribution statement

Marco Boetti: Conceptualization, Methodology, Software, Formal analysis, Investigation, Resources, Data curation, Writing – original draft, Writing – review & editing, Visualization. **Lilly Verso:** Conceptualization, Methodology, Formal analysis, Resources, Data curation, Writing – original draft, Writing – review & editing.

Declaration of competing interest

The authors declare that they have no known competing financial interests or personal relationships that could have appeared to influence the work reported in this paper.

Acknowledgements

We are grateful to Alex Liberzon and Maarten van Reeuwijk for the valuable help with this study and to the members of the Turbulence Structure Laboratory at Tel Aviv University for their assistance with the experiments.

This work was supported by the COMPLETE project (European Union Horizon 2020 Research and Innovation Programme under the Marie Sklodowska-Curie Action, Grant Agreement No. 675675). The computational resources required for this project were supported by the Cy-Tera Project (NEA ΥΠΟΔΟΜΗ/ΣΤΡΑΤΗ/0308/31), which is co-funded by the European Regional Development Fund and the Republic of Cyprus through the Research Promotion Foundation. The authors acknowledge support by Israel Science Foundation Grant no. 945/15.

Table A.3
Characteristics of test runs in linearly stratified flow.

	Test A	Test B	Test C
a/a^{P_1}	0.5	0.5	1
$\rho_p/\rho_p^{P_1}$	1	1	1
$\gamma a/\rho_p$	1.2510^{-4}	7.110^{-5}	8.110^{-5}
Fr_D	5.1	5.7	13.3

Appendix. Linear stratification

The new algorithm is tested in linearly stratified fluid and then compared with two models (Yick et al., 2009; Doostmohammadi et al., 2014) specifically developed for that stratification environment. These models reproduce F_S as an additional drag term as: $\mathbf{F_S} = 0.5C_D^S\rho_f A_p |\mathbf{v}_{rel}|\mathbf{v}_{rel}$.

The stratification-induced drag coefficient C_D^S is defined as: $C_D^S = 1.9C_D Ri^{1/2}$ (Yick et al., 2009) and $C_D^S = 0.67C_D Ri^{1/2}$ (Doostmohammadi et al., 2014), being $Ri = Re/Fr^2 = a^3N_{Doost}^2/\nu\upsilon$ the Richardson number and $N_{Doost} = \sqrt{g\gamma/\rho(z_0)}$ the Brunt–Vaisala frequency.

The main results of the comparison are shown in Fig. 8. Three runs are performed by varying the particle diameter a and the fluid density slope $\gamma = |d\rho_f/dz|$, as reported in Table A.3. The Froude number Fr_{Doost} (used to retrieve V_{cw}) is computed similarly to Doostmohammadi et al. (2014) as: $Fr_{Doost} = \upsilon_{St}/N_D a$, being $\upsilon_{St} = ga^2(\rho_p - \rho_f(z_0))/(18\nu\rho(z_0))$ the Stokes velocity.

In Fig. 8a–c is presented the stratification force vertical profiles scaled using the particle diameter. Differently from Yick et al. (2009) and Doostmohammadi et al. (2014), in the new model F_S is slower to adjust to the surrounding flow. This is due to the initialization of τ_{cross} and the caudal wake density, which is set to $\rho_{cw} = \rho_f(t=0)$. When $t > \tau_{cross}$, the stratification force "forgets" the imposed initial conditions and the three models have the same monotonic decreasing behaviour. From the tests presented in Fig. 8a–c seems that our algorithm produce a F_S in-between the models of Doostmohammadi et al. (2014) and Yick et al. (2009). The resulting vertical velocity, Fig. 8d–f, shows similar profiles with Doostmohammadi et al. (2014) and Yick et al. (2009), in particular when $t > \tau_{cross}$.

References

Abaid, N., Adalsteinsson, D., Agyapong, A., McLaughlin, R., 2004. An internal splash: Levitation of falling spheres in stratified fluids. Phys. Fluids 16 (5), 1567–1580.

Ardekani, A., Doostmohammadi, A., Desai, N., 2017. Transport of particles, drops, and small organisms in density stratified fluids. Phys. Rev. Fluids 2 (10), 100503.

Bayareh, M., Doostmohammadi, A., Dabiri, S., Ardekani, A.M., 2013. On the rising motion of a drop in stratified fluids. Phys. Fluids 25 (10), 103302, URL https://doi.org/10.1063/1.4823724.

Boetti, M., van Reeuwijk, M., Liberzon, A., 2021. Potential-enstrophy lengthscale for the turbulent/nonturbulent interface in stratified flow. Phys. Rev. Fluids 6 (11), 114803.

Burd, A., Jackson, G., 2009. Particle aggregation. Annu. Rev. Mar. Sci. 1, 65–90.

Camassa, R., Harris, D., Hunt, R., Kilic, Z., McLaughlin, R., 2019. Cluster formation and self-assembly in stratified fluids: a novel mechanism for particulate aggregation. arXiv preprint:1905.07610.

Camassa, R., Khatri, S., McLaughlin, R., Prairie, J., White, B., Yu, S., 2013. Retention and entrainment effects: Experiments and theory for porous spheres settling in sharply stratified fluids. Phys. Fluids 25 (8), 081701.

Camilli, R., Reddy, C., Yoerger, D., Van Mooy, B., Jakuba, M., Kinsey, J., McIntyre, C., Sylva, S., Maloney, J., 2010. Tracking hydrocarbon plume transport and biodegradation at deepwater horizon. Science 330 (6001), 201–204.

Candelier, F., Mehaddi, R., Vauquelin, O., 2014. The history force on a small particle in a linearly stratified fluid. J. Fluid Mech. 749, 184–200.

Deepwell, D., Ouillon, R., Meiburg, E., Sutherland, B., 2021. Settling of a particle pair through a sharp, miscible density interface. Phys. Rev. Fluids 6 (4), 044304.

Dejoan, A., Monchaux, R., 2013. Preferential concentration and settling of heavy particles in homogeneous turbulence. Phys. Fluids 25 (1), 013301, URL https://doi.org/10.1063/1.4774339.

Doostmohammadi, A., Dabiri, S., Ardekani, A.M., 2014. A numerical study of the dynamics of a particle settling at moderate Reynolds numbers in a linearly stratified fluid. J. Fluid Mech. 750, 5–32.

Eames, I., Hunt, J., 1997. Inviscid flow around bodies moving in weak density gradients without buoyancy effects. J. Fluid Mech. 353, 331–355.

Elghobashi, S., 1991. Particle-laden turbulent flows: direct simulation and closure models. Appl. Sci. Res. 48, 301–314. http://dx.doi.org/10.1007/BF02008202, URL https://doi.org/10.1007/BF02008202.

Geller, A., Lee, S., Leal, L., 1986. The creeping motion of a spherical particle normal to a deformable interface. J. Fluid Mech. 169, 27–69.

Kok, J., 2011. A scaling theory for the size distribution of emitted dust aerosols suggests climate models underestimate the size of the global dust cycle. Proc. Natl. Acad. Sci. 108 (3), 1016–1021.

Lange, M., van Sebille, E., 2017. Parcels v0. 9: prototyping a Lagrangian ocean analysis framework for the petascale age. Geosci. Model Dev. 10 (11), 4175–4186.

Long, R.R., 1978. Theory of turbulence in a homogeneous fluid induced by an oscillating grid. Phys. Fluids 21 (10), 1887–1888, URL https://aip.scitation.org/doi/abs/10.1063/1.862087.

MacIntyre, S., Alldredge, A., Gotschalk, C., 1995. Accumulation of marines now at density discontinuities in the water column. Limnol. Oceanogr. 40 (3), 449–468.

Magnaudet, J., Mercier, M., 2020. Particles, drops, and bubbles moving across sharp interfaces and stratified layers. Annu. Rev. Fluid Mech. 52, 61–91.

Mandel, T., Waldrop, L., Theillard, M., Kleckner, D., Khatri, S., et al., 2020. Retention of rising droplets in density stratification. Phys. Rev. Fluids 5 (12), 124803.

Maxey, M.R., Riley, J.J., 1983. Equation of motion for a small rigid sphere in a nonuniform flow. Phys. Fluids 26 (4), 883–889.

McAdam, R., van Sebille, E., 2018. Surface connectivity and interocean exchanges from drifter-based transition matrices. J. Geophys. Res. Oceans 123 (1), 514–532.

Meller, Y., Liberzon, A., 2016. Particle data management software for 3dparticle tracking velocimetry and related applications–the flowtracks package. J. Open Res. Softw. 4 (1).

Michallet, H., Mory, M., 2004. Modelling of sediment suspensions in oscillating grid turbulence. Fluid Dyn. Res. 35, 87–106, URL https://hal.archives-ouvertes.fr/hal-00260290.

OpenPTV consortium, 2014. Open source particle tracking velocimetry. URL http://www.openptv.net/.

Pierson, J., Magnaudet, J., 2018. Inertial settling of a sphere through an interface. Part 1. From sphere flotation to wake fragmentation. J. Fluid Mech. 835, 762–807.

van Reeuwijk, M., Jonker, H., Hanjalic, K., 2008a. Wind and boundary layers in Rayleigh-benard convection. I. Analysis and modeling. Phys. Rev. E 77 (3), 036311.

van Reeuwijk, M., Jonker, H., Hanjalic, K., 2008b. Wind and boundary layers in Rayleigh-benard convection. II. Boundary layer character and scaling. Phys. Rev. E 77 (3), 036312.

Riley, J.J., Lelong, M.-P., 2000. Fluid motions in the presence of strong stable stratification. Annu. Rev. Fluid Mech. 32 (1), 613–657, URL https://doi.org/10.1146/annurev.fluid.32.1.613.

Shnapp, R., Shapira, E., Peri, D., Bohbot-Raviv, Y., Fattal, E., Liberzon, A., 2019. Extended 3D-PTV for direct measurements of Lagrangian statistics of canopy turbulence in a wind tunnel. Sci. Rep. 9 (7405), http://dx.doi.org/10.1038/s41598-019-43555-2, URL https://doi.org/10.1038/s41598-019-43555-2.

Smith, D., Simon, M., Alldredge, A., Azam, F., 1992. Intense hydrolytic enzyme activity on marine aggregates and implications for rapid particle dissolution. Nature 359 (6391), 139–142.

Squires, K.D., Eaton, J.K., 1991. Preferential concentration of particles by turbulence. Phys. Fluids A 3 (5), 1169–1178.

Srdić-Mitrović, A., Mohamed, N., Fernando, H., 1999. Gravitational settling of particles through density interfaces. J. Fluid Mech. 381, 175–198.

Stout, J., Arya, S., Genikhovich, E., 1995. The effect of nonlinear drag on the motion and settling velocity of heavy particles. J. Atmos. Sci. 52 (22), 3836–3848.

Traugott, H., Hayse, T., Liberzon, A., 2011. Resuspension of particles in an oscillating grid turbulent flow using PIV and 3D-PTV. In: Journal of Physics: Conference Series, Vol. 318. IOP Publishing, 052021.

Turco, R., Toon, O., Ackerman, T., Pollack, J., Sagan, C., 1983. Nuclear winter: Global consequences of multiple nuclear explosions. Science 222 (4630), 1283–1292.

Verso, L., 2020. Particles Crossing Density Interfaces (Ph.D. thesis). Tel Aviv University.

Verso, L., van Reeuwijk, M., Liberzon, A., 2017. Steady state model and experiment for an oscillating grid turbulent two-layer stratified flow. Phys. Rev. Fluids 2, 104605.

Verso, L., van Reeuwijk, M., Liberzon, A., 2019. Transient stratification force on particles crossing a density interface. Int. J. Multiph. Flow. 121, 103109.

Verstappen, R., Veldman, A., 2003. Symmetry-preserving discretization of turbulent flow. J. Comput. Phys. 187 (1), 343–368.

Wang, L.-P., Maxey, M.R., 1993. Settling velocity and concentration distribution of heavy particles in homogeneous isotropic turbulence. J. Fluid Mech. 256, 27–68.

White, F., 2006. Viscous Fluid Flow, third ed. McGraw-Hill, Boston.

Woods, A., 1995. The dynamics of explosive volcanic eruptions. Rev. Geophys. 33 (4), 495–530.

Yick, K., Torres, C., Peacock, T., Stocker, R., 2009. Enhanced drag of a sphere settling in a stratified fluid at small Reynolds numbers. J. Fluid Mech. 632, 49–68.

Zvirin, Y., Chadwick, R., 1975. Settling of an axially symmetric body in a viscous stratified fluid. Int. J. Multiph. Flow. 1 (6), 743–752.